

Three-dimensional flow structures of straight rough-bed channels with different aspect ratios

Y. Takakuwa

Graduate School of Science and Engineering, Chuo University, Tokyo, Japan

S. Fukuoka

Research and Development Initiative, Chuo University, Tokyo, Japan

ABSTRACT: It is significant in hydraulic engineering to clarify the relationship between flow structures, channel width and bed roughness. In this paper, three-dimensional numerical experiments were conducted about turbulent flows over rectangular straight rough-bed channels with different aspect ratios (0.36 ~ 1.38) and relative depths on the roughness height (3.63 ~ 12.00). Characteristics of secondary flows in rough-bed channel and mutual relations of the outer secondary flow, the inner secondary flow and the bottom secondary flow were investigated in detail. The velocity-dip phenomenon occurred when the aspect ratio was larger than 0.84 and the relative depth was smaller than 4.18, and did not occur when the aspect ratio was smaller than 0.39 and the relative depth was larger than 4.88.

1 INTRODUCTION

In the field of hydraulic engineering, it is important to clarify the relationship between flow structures, channel aspect ratio (b/h , b = channel width; h = channel depth), and relative depth (h/r , r = roughness height) in order to understand flow resistance and three-dimensional flow structures.

Hayashi et al. (2006) conducted the direct numerical simulation in smooth-bed channel with aspect ratio 2.0. They found three kinds of secondary flows in the smooth-bed channel. Figure 1 shows an outline drawing of the secondary flows by reference to the results of Hayashi et al. (2006). Secondary flows toward a corner at the channel bottom are divided into the bottom secondary flow along the channel bottom and the outer secondary flow rising along the sidewall. The outer secondary flow transports slow water from the bottom corner to the channel center of the free surface. Therefore, the free surface velocity in the channel center becomes small and the maximum streamwise velocity appears below the free surface (velocity-dip phenomenon). Simultaneously, the inner secondary flow which rotates in the opposite direction to the outer secondary flow generates at the corner surrounded by the free surface and the sidewall.

Nezu & Nakagawa (1993) clarified the generation of the outer secondary flow and bottom secondary flow irrespective of the aspect ratio by the experiments of smooth channel with the aspect ratio 2.0 or more, and also clarified the maximum secondary flow velocity was 1.5 ~ 3.0% of the maximum streamwise velocity. Greg et al. (1995) showed generation of three kinds of secondary flows in experimental and numerical study using the rectangular smooth channel where the aspect ratio is less than 1.0. Joung & Choi (2010) found by the direct simulation in the smooth-bed channel with the aspect ratio 1.0 that directions of inner secondary flow and outer secondary flow were closely related to instantaneous vertical velocity and coherent structures of the ejection and sweep along the sidewall.

There are few researches concerning effects of the aspect ratio and roughness on secondary flows in rough-bed channels. Tominaga & Nezu (1986) experimentally showed that the

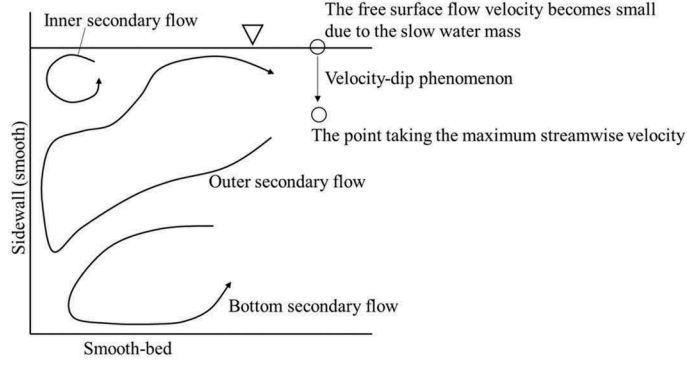


Figure 1. Schematic drawing showing bottom, outer and inner secondary flows and the velocity-dip phenomenon in the smooth-bed channel by reference to the results of Hayashi et al. (2006).

maximum secondary flow velocity became large (roughly 3 to 4% of the maximum streamwise velocity) in rough-bed channels with different aspect ratios ($b/h = 2.00 \sim 8.00$) and relative depths ($h/r = 6.67 \sim 26.3$), and that secondary flows were observed even at a transverse position more than 2.5 times channel depth away from the sidewall. Little consideration, however, has been given to effects of aspect ratio and roughness on flow structures over rectangular straight rough-bed channels.

In this study, we performed three-dimensional numerical experiments on steady flows in rectangular straight rough-bed channels with extremely narrow widths ($b/h = 0.36 \sim 1.38$) and large bottom roughness elements ($h/r = 3.63 \sim 12.00$). First, we investigated effects of the aspect ratio and the relative depth on scales of secondary flows, and discussed where the maximum streamwise flow velocity occurred. Second, we examined relationships between secondary flows and flows rising or sinking around roughness elements, and clarified three-dimensional flow structures near the channel bottom in extremely narrow rough-bed channels.

2 NUMERICAL METHOD

2.1 Calculation of fluid motion

Fluid motions are calculated using the APM (Fukuoka et al. 2014) in the Cartesian coordinate system. Basic equations of fluid motions are described as follows. SGS stresses are evaluated by the Smagorinsky model.

$$\frac{\partial u_i}{\partial x_i} = 0 \quad (1)$$

$$\frac{Du_i}{Dt} = g_i - \frac{1}{\rho} \frac{\partial P}{\partial x_i} + \frac{\partial}{\partial x_j} \{2(\nu + \nu_t)S_{ij}\} \quad (2)$$

$$S_{ij} = \frac{1}{2} \left(\frac{\partial u_i}{\partial x_j} + \frac{\partial u_j}{\partial x_i} \right) \quad (3)$$

$$\nu_t = (C_S \Delta)^2 \sqrt{2S_{ij}S_{ij}} \quad (4)$$

where x_i = Cartesian coordinate; u_i = i th component of mass averaged velocity; P = sum of the pressure and isotropic component of SGS stress; g_i = i th component of gravitational

acceleration; ρ = volume averaged density; ν = kinematic viscosity; ν_t = SGS turbulent viscosity; S_{ij} = strain rate tensor; C_S = Smagorisky constant (≈ 0.173); Δ = grid size.

Advection terms in the Equation 2 are solved by upwind differences of the third order accuracy, time advancement is achieved by the SMAC method, and pressure convergence is calculated by the SOR method. The free-surface variation is analyzed using the VOF method (Hirt & Nichols 1981).

2.2 Methodology of fluid calculation for grids containing the channel surface

Figure 2a shows the methodology of fluid calculation for grids containing channel surfaces, and these grids are dealt as solid-liquid mixed fluid (Ushijima et al. 2008). The mass and momentum of solid-liquid mixed fluid are evaluated using the volume fraction of the solid phase α as shown in Equations 5 and 6.

$$\rho = \alpha\rho_s + (1 - \alpha)\rho_f \quad (5)$$

$$\rho u_i = \alpha\rho_s u_{s,i} + (1 - \alpha)\rho_f u_{f,i} \quad (6)$$

where suffix s and f denote the solid and the liquid phase, respectively.

The volume fraction of the solid phase influences evaluation of the velocity of mixed fluid directly, and its precision has large influences on the velocity distribution in the vicinity of boundaries. The volume fraction of the solid phase is evaluated using the subcell method (see Figure 2b).

3 NUMERICAL EXPERIMENTS AND CALCULATION CONDITIONS

3.1 Concepts of numerical experiments

Three-dimensional numerical experiments were conducted about turbulent flows which have same discharge per unit width in rectangular straight rough-bed channels with different aspect ratios ($b/h = 0.36 \sim 1.38$) and relative depths on the roughness height ($h/r = 3.63 \sim 12.00$). Figure 3 and Table 1 show channel schemes and hydraulic conditions, respectively. In the case 1 ($b/h = 0.36$), a steady flow ($Q = 0.06$ l/s) was supplied in the channel with 2 m long, 7 mm width and 1/20 bed slope, following to the experiment by Ancy et al. (2002). Bottom roughness of the channel was given by cylinders of uniform size. In the paper of Ancy et al. (2002), the size of cylinder was not clearly described, so that the

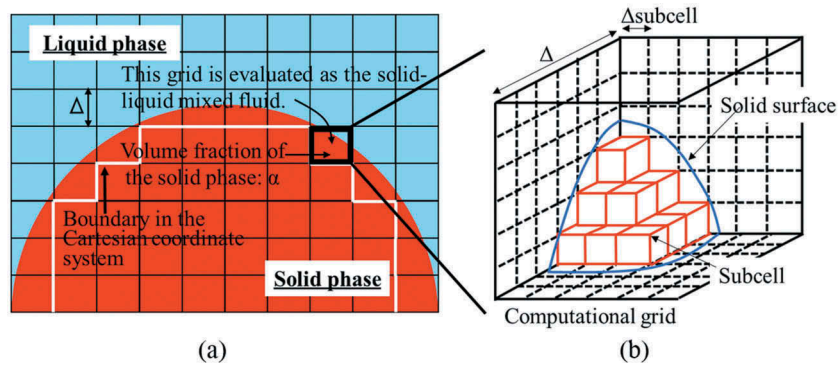


Figure 2a. Methodology of fluid calculation for grids containing the channel surface using the one-fluid model of solid-liquid multiphase. Figure 2b. Concept of the subcell method to evaluate the volume fraction of the solid phase in a computational grid.

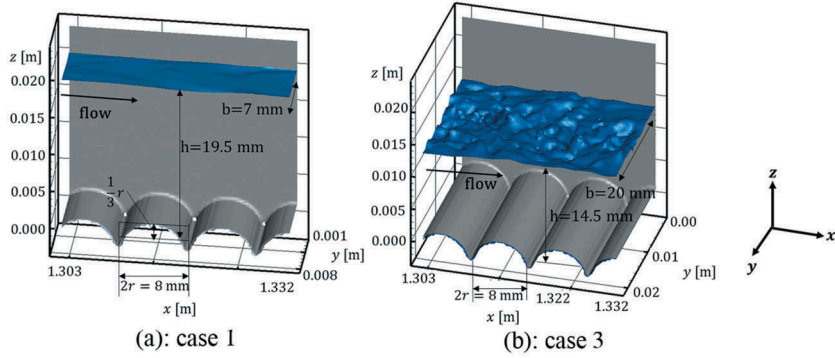


Figure 3. Channel schemes of case 1 and 3. The origin of the coordinate was set $r/3$ lower than the top of cylinders.

diameter of cylinders was set to $2r = 8$ mm to satisfy the experimental channel depth $h = 20$ m. The origin of the coordinate was set $r/3$ lower than the top of cylinders.

Case 2 and 3 were analyzed under the similar conditions to case 1. Discharges per unit width were set equal to that of case 1. Case 4 with small roughness ($2r = 3$ mm) at the bed and the same channel width as case 1 was analyzed in order to estimate the effect of roughness sizes on flow structures.

The velocity distribution at $x = 0.20$ m was given to the upstream boundary condition in every step to make the boundary layer develop in the short distance. At the downstream end, channel depth was controlled by giving the channel depth at the upstream point by one step.

3.2 Calculation conditions and measurements of the turbulent flow

Our previous research (Takakuwa & Fukuoka 2019) showed that flow structures over the permeable fixed rough-bed could be analyzed with sufficient accuracy by the APM under following conditions. First, the computational grid size Δ must be less than $1/10$ of the roughness diameter. Second, the subcell size Δ_{subcell} should be less than $1/6$ of the grid size Δ to accurately evaluate the volume fraction of the solid phase including in a computational grid (see Figure 2b).

In this paper, according to these conditions, grid sizes and subcell sizes were set to $\Delta = \Delta_x = \Delta_y = \Delta_z = 0.3$ mm and $\Delta_{\text{subcell}} = 0.05$ mm, respectively. Time step for each case was set to 2.0×10^{-5} s.

Table 1. Channel and hydraulic conditions, where Q = discharge; R = hydraulic radius; h = channel depth; b = channel width; b/h = aspect ratio; r = height of roughness element; h/r = relative depth on roughness height; \bar{u}_{max} = maximum value of the mean streamwise velocity; U_{mean} = bulk velocity; $U^*(R)$ = friction velocity; Re = Reynolds number on the hydraulic radius and the bulk velocity; Fr = Froude number on the hydraulic radius and the bulk velocity; $|sv_{\text{max}}|$ = maximum size of the mean secondary flow velocity.

	Q [l/s]	R [mm]	h [mm]	b [mm]	b/h [-]	r [mm]	h/r [-]	\bar{u}_{max} [m/s]	U_{mean} [m/s]	$U^*(R)$ [m/s]	Re [-]	Fr [-]	SV_{max} [m/s]	$ SV_{\text{max}} /\bar{u}_{\text{max}}$ [-]
Case 1	0.06	2.97	19.5	7	0.36	4.0	4.88	0.68	0.44	0.038	1.3E+03	2.58	0.04	0.06
Case 2	0.11	4.93	16.7	14	0.84	4.0	4.18	0.78	0.47	0.049	2.3E+03	2.14	0.07	0.09
Case 3	0.17	5.92	14.5	20	1.38	4.0	3.63	0.88	0.59	0.054	3.5E+03	2.43	0.07	0.08
Case 4	0.06	2.93	18.0	7	0.39	1.5	12.00	0.68	0.48	0.038	1.4E+03	2.81	0.03	0.04

Measurements of turbulent flows in the APM were performed according to Nezu (1977). The sampling time step was set to 4.0×10^{-4} s, and the total number of sampling for each point was 2500 (1 second measurement). It was confirmed that structures of time-averaged flows were almost the same as those measured for 2 seconds (case 3).

4 RESULTS AND DISCUSSIONS

4.1 *Time-averaged flow structures in a cross-section*

Figures 4i and 4ii show cross-sectional distributions of the time-averaged streamwise velocity and the time-averaged secondary flow velocity at a top section of roughness element of case 1 ~ case 4. Three kinds of secondary flows appear in case 1, 2, and 4 of rough-bed channels as well as the secondary flows in a smooth-bed channel (Figure 4ii of case Hayashi et al. 2006). On the other hand, in case 3 where the relative depth h/r is the smallest, the outer and bottom secondary flows occur, but no inner secondary flows are formed at corners near the free surface. Focusing on the streamwise velocity, velocity-dip phenomena occur in case 2 and 3, but not in case 1 and 4 where aspect ratios are quite small. The reasons are described below.

In cases 2 and 3 where aspect ratios are not small compared to case 1 and 4, outer secondary flows proceed to the channel center after reaching the free surface where the slow water mass from the bottom corner to the channel center of the free surface is transported as shown in Figure 1. The free surface flow velocity in the channel center becomes small, and the velocity-dip phenomenon occurs.

Figure 4iii shows an outline drawing of the secondary flows in the extremely narrow channel. The outer secondary flow is formed at considerably lower position. Although the weak upward flow of the outer secondary flow rises along the sidewall, but do not reach the free surface.

Therefore, in cases 1 and 4, the maximum streamwise velocity appears at the channel center on the free surface, and velocity-dip phenomena do not occur.

As mentioned above, the scale of the outer secondary flow and the position where the maximum streamwise velocity appears are closely related. As seen in respective cases 1 and 4 of Figure 4, outer secondary flows expand from the bottom $z = 0$ to $z = 8$ and 7 mm. In case 1 where the relative depth ($h/r = 4.88$) is smaller than that of case 4 ($h/r = 12.00$), it is probable that the upward flow along the sidewall is strong and the outer secondary flow spreads to rather high position. These outer secondary flows eventually develop to higher positions (case 1: 82% of the channel depth, case 4: 67%). In case 3 where the relative depth h/r is 3.63 and the aspect ratio b/h is 1.38, the outer secondary flow rises along the side wall to the free surface, and the inner secondary flow could not occur.

4.2 *Longitudinal variation of secondary flows within a cross-section*

Figure 5 shows the schematic drawing of three-dimensional structures near the channel bottom in a rough-bed channel. As shown in solid arrows near the cylinder roughness element, the flow over bottom roughness element collides with the adjoining roughness element and is divided into the downward flow sinking into the valley between roughness elements (sinking flow, position c in Figure 5) and the upward flow rising to a higher position (rising flow, position d in Figure 5). Outer and bottom secondary flows merged with these vertical flows, and secondary flow structures change longitudinally.

At the position c, the upward component of the outer secondary flow along the sidewall is weakened by the sinking flow, and the upward flow velocity becomes small as shown by the dashed line in Figure 5. The downward component of the bottom secondary flow near the bottom corner is strengthened by the sinking flow, and the downward flow velocity becomes large. In addition, the upward component of the bottom secondary flow near the channel center is weakened by the sinking flow.

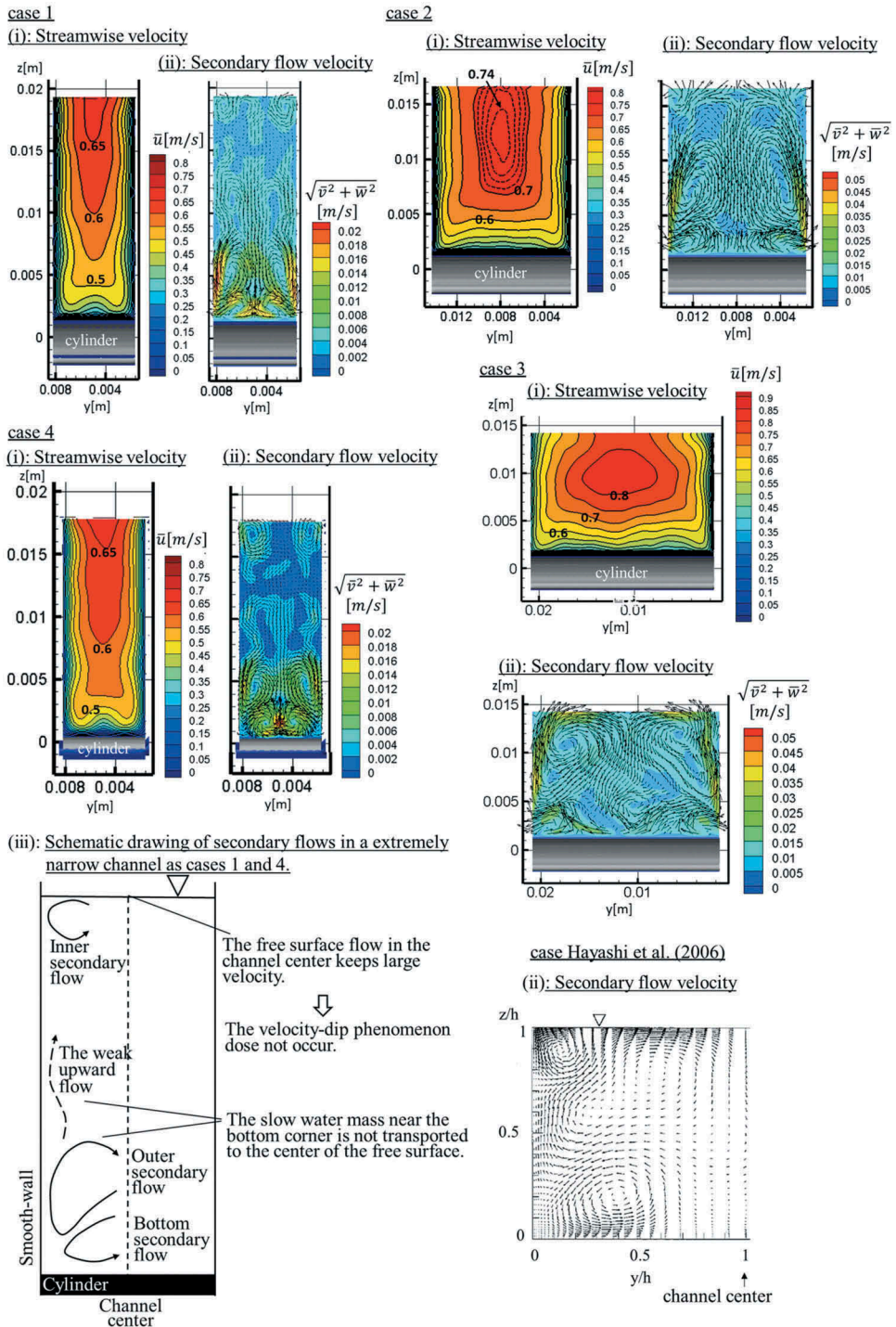


Figure 4. Mean streamwise velocities and mean secondary flow velocities within cross-sections of top of roughness element. i and ii of all cases show distributions of streamwise velocity and secondary flow velocity, respectively. In i of case 2, broken lines indicate the detail distribution of streamwise velocity. ii of case Hayashi et al. (2006) shows the distribution of secondary flows in a smooth-bed channel, cited from Left half of the Figure 7 of Hayashi et al. (2006) and partially modified. iii shows a schematic drawing of secondary flows in the extremely narrow channel.

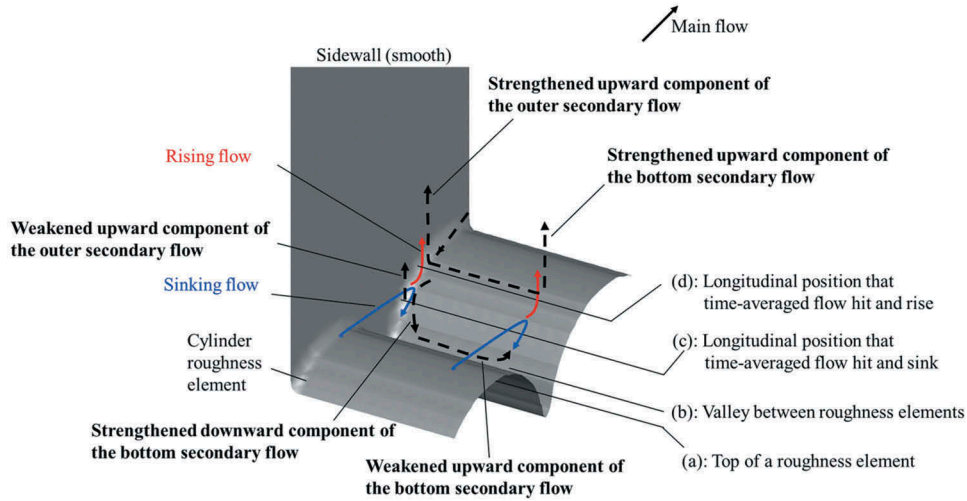


Figure 5. Schematic drawing showing three-dimensional structures of time-averaged flows near the channel bottom in a rough-bed channel. Blue solid arrows indicate the flow sinking into the valley between roughness elements. Red solid arrows indicate the flow rising after hit with a cylinder roughness element. Dashed arrows indicate outer and bottom secondary flows affected by the sinking flow and the rising flow.

At the position d, the upward components of outer and bottom secondary flows are strengthened by the rising flow.

Figure 6 shows longitudinal variations of secondary flows (\bar{v} , \bar{w}) of cases 2 and 4. Contours indicate the secondary flow velocity $(\bar{v}^2, \bar{w}^2)^{0.5}$. Figure number a ~ d in Figure 6 correspond to the longitudinal positions on the roughness element of Figure 5. In case 2 with the relative depth of $h/r = 4.18$, the maximum size $|SV_{\max}|$ of the secondary flow velocity near the roughness element becomes 9% of the maximum streamwise velocity \bar{u}_{\max} . In case 4 where the relative depth h/r is 12.00, the ratio $|SV_{\max}|/\bar{u}_{\max}$ is 0.04 and is similar to values ($|SV_{\max}|/\bar{u}_{\max} = 0.03 \sim 0.04$) of rough-bed channels with relative depths ($h/r = 6.67 \sim 26.3$) conducted by Tominaga & Nezu (1986). When the relative depth further increases, the ratio $|SV_{\max}|/\bar{u}_{\max}$ is considered to approach the value of the smooth-bed channel ($|SV_{\max}|/\bar{u}_{\max} = 0.015 \sim 0.03$, Nezu & Nakagawa 1993).

Vertical ranges of secondary flows are limited to $z = 1.1 r$ and $0.75 r$ ($h/r = 4.18$ and 12.00, respectively) from the top of the roughness element as shown in solid lines.

5 CONCLUSIONS

Following conclusions were obtained.

1. The flow sinking into the valley between roughness elements and the flow rising the roughness element occur near the bottom in a rough-bed channels. Outer and bottom secondary flows merged with these vertical flows, and secondary flow structures near the channel bed change longitudinally. The ratio $|SV_{\max}|/\bar{u}_{\max}$ of the rough-bed channel with the small relative depth becomes larger than that of the smooth-bed channel. When the relative depth increases and the effect of roughness elements decrease, the value $|SV_{\max}|/\bar{u}_{\max}$ approaches that of the smooth-bed channels.
2. Scales of outer secondary flows and bottom secondary flows are spread in the range from the top of the roughness element to the height of a radius of the bottom cylinder, and secondary flow structures above that height are almost longitudinally uniform.
3. The velocity-dip phenomenon occurred when the aspect ratio was larger than 0.84 and the relative depth was smaller than 4.18. When the aspect ratio was smaller than 0.39 and the relative depth was larger than 4.88, outer secondary flows did not reach the free surface and the velocity-dip phenomenon did not occur.

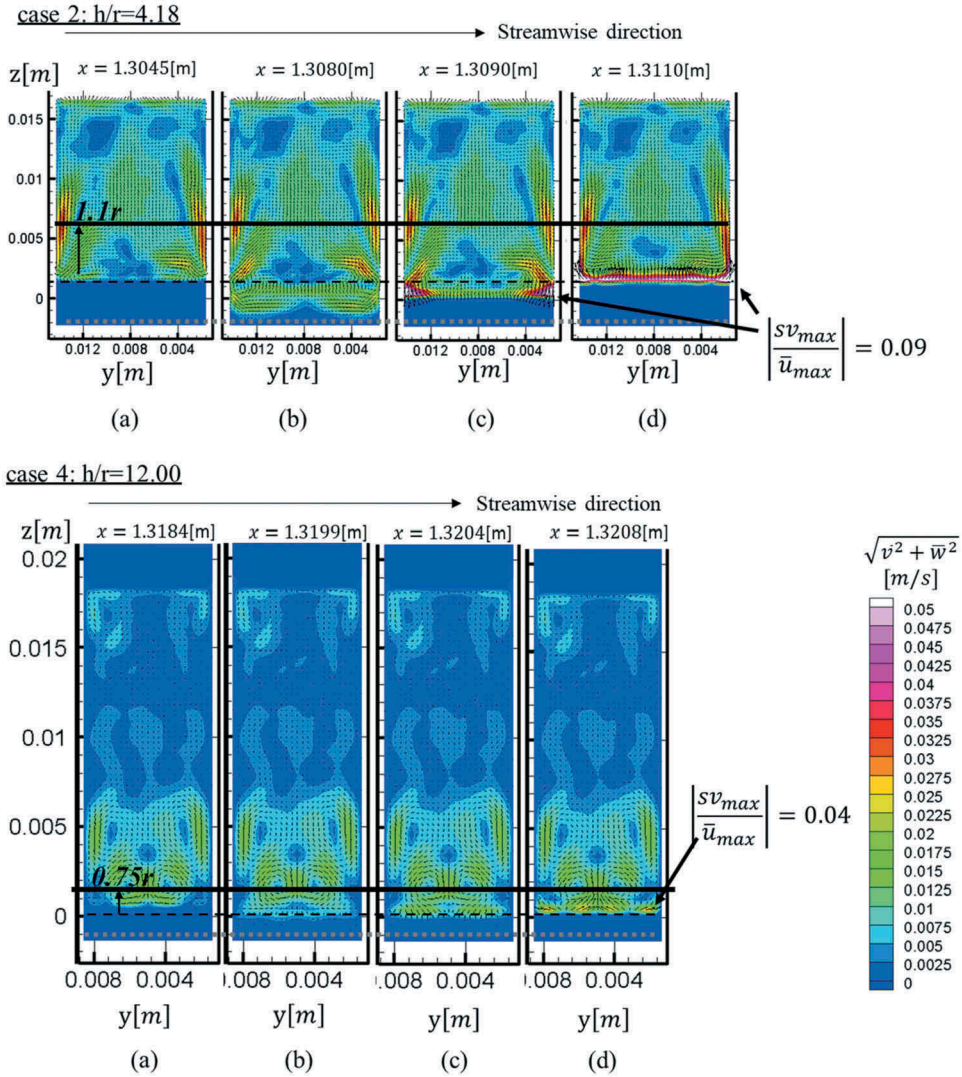


Figure 6. Longitudinal variation of secondary flows of cases 2 and 4. Streamwise positions of cross-section views a, b, c, and d correspond to longitudinal positions of Figure 5. Solid lines, broken lines and dotted lines of cases 2 and 4 show heights that secondary flows change in streamwise direction, heights of roughness top, and heights of the valley between cylinders, respectively.

REFERENCES

- Ancey, C., Bigillon, F., Frey, P., Lanier, J. & Ducret, R. 2002. Saltating motion of a bead in a rapid water stream. *Phys. Rev. E* 66: 036306.
- Fukuoka, S., Fukuda, T. & Uchida, T. 2014. Effects of sizes and shapes of gravel particles on sediment transports and bed variations in a numerical movable-bed channel. *Adv. Water Resour.* 72: 84–96.
- Grega, L.M., Wei, T., Leighton, R.I. and Neves, J.C. 1995. Turbulent mixed-boundary flow in a corner formed by a solid wall and a free surface. *J. Fluid Mech.* 294: 17–46.
- Hayashi, S., Ohmoto, T. & Honda, I. 2006. Direct numerical simulation of secondary currents and vortex structures in an open channel flow. *J. JSCE B.* 62(1): 80–99. (in Japanese).
- Hirt, C.W. & Nichols, B.D. 1981. Volume of fluid (VOF) method for the dynamics of free boundaries. *J. Comput. Phys.* 39: 201–225.

- Joung, Y. Choi, S. 2010. Direct numerical simulation of low Reynolds number flows in an open-channel with sidewalls. *Int. J. Numer. Meth. Fluids*. 62: 854–874.
- Nezu, I. 1977. Turbulent structure in open-channel flows. Ph.D. thesis, Kyoto University.
- Nezu, I. & Nakagawa, H. 1993. *Turbulence in Open-Channel Flows*. IAHR-monograph, CRC Press, Rotterdam: The Netherlands.
- Tominaga, A. & Nezu, I. 1986. Three-dimensional turbulent structure in a straight open-channel flow with varying boundary roughness. *Proc. of 3rd Asian Congress of Fluid Mech.* 608–611. Tokyo.
- Takakuwa, Y. & Fukuoka, S. 2019. Structures of flow with particles saltating over the permeable fixed rough bed. *Proc. Two-phase modeling for Sediment Dynamics in Geophysical flows THESIS-2019*, Delaware – USA.
- Ushijima, S., Fukutani, A. & Makino, O. 2008. Prediction method for movements with collisions of arbitrary-shaped objects in 3D free-surface flows. *J. JSCE B*. 64(2): 128–138. (*in Japanese*).